Check for updates

Nanoparticle single-cell multiomic readouts reveal that cell heterogeneity influences lipid nanoparticle-mediated messenger RNA delivery

Curtis Dobrowolski [1,5], Kalina Paunovska [1,5], Elisa Schrader Echeverri[1], David Loughrey[1],
Alejandro J. Da Silva Sanchez[2,3], Huanzhen Ni[1], Marine Z. C. Hatit [1], Melissa P. Lokugamage[1],
Yanina Kuzminich [2,4], Hannah E. Peck[1], Philip J. Santangelo [1] and James E. Dahlman [1]✉

Cells that were previously described as homogeneous are composed of subsets with distinct transcriptional states. However, it remains unclear whether this cell heterogeneity influences the efficiency with which lipid nanoparticles (LNPs) deliver messenger RNA therapies in vivo. To test the hypothesis that cell heterogeneity influences LNP-mediated mRNA delivery, we report here a new multiomic nanoparticle delivery system called single-cell nanoparticle targeting-sequencing (SENT-seq). SENT-seq quantifies how dozens of LNPs deliver DNA barcodes and mRNA into cells, the subsequent protein production and the transcriptome, with single-cell resolution. Using SENT-seq, we have identified cell subtypes that exhibit particularly high or low LNP uptake as well as genes associated with those subtypes. The data suggest that cell subsets have distinct responses to LNPs that may affect mRNA therapies.

n humans, lipid nanoparticles (LNPs) have been used to deliver messenger RNA to antigen-presenting cells after intramuscular administration[1,2], mRNA encoding Cas9 and single guide RNA (sgRNA) to hepatocytes after systemic administration[3], and short interfering RNA (siRNA) to hepatocytes after systemic administration[4]. These advances are tempered by clinical setbacks in which nanoparticle-mediated mRNA delivery was insufficient to treat disease[5–7], underscoring the potential impact of LNPs with improved efficacy. To improve LNPs, scientists have formulated them with chemically diverse lipids identified in vitro[8] (cell culture) or in vivo[9] (adult mammals). These efforts have led to LNPs that deliver mRNA to the lung, spleen and immune cells in preclinical models[10–17].

In addition to lipid design, clinical RNA delivery has required scientists to understand genes that influence drug delivery in vivo. In one example, LNPs were shown to deliver siRNA into hepatocytes expressing low-density lipoprotein receptor by interacting with serum apolipoprotein E in mice[18]. This endogenous apolipoprotein E-mediated mechanism was used in a Food and Drug Administration (FDA)-approved LNP–siRNA therapy[19] and in a recent phase 1 clinical trial[3]. Similarly, after siRNA conjugated to modified *N*-acetylgalactosamine (GalNAc) was shown to enter hepatocytes by binding the asialoglycoprotein receptor (ASGPR) in mice[20], GalNAc conjugates were used in FDA- and/or European Medicines Agency-approved medicines[21–23] and to generate other promising clinical data[24,25]. Taken together, these data demonstrate that preclinical studies to identify the biological mechanism of delivery are often necessary for clinical RNA delivery[26]. More recently, preclinical LNP-mediated mRNA delivery has been doubled[27] or reduced to nearly zero[28,29] by treating cells with small molecules that manipulate endocytic, inflammatory or metabolic signalling, indicating that these cellular processes affect LNP

delivery by yet-to-be-determined mechanisms. Coupled with reports that nearly all RNA can be retained in endosomes after delivery[30,31], these data suggest that pathways can affect LNP biodistribution and, separately, the functional delivery of RNA payloads.

Research into the biology of LNP delivery faces two key limitations, however. First, candidate genes are often identified using in vitro nanoparticle delivery. Because in vitro nanoparticle delivery does not always replicate in in vivo nanoparticle delivery experiments[32], we reasoned that an unbiased in vivo approach could reveal alternative gene candidates. Second, the extent to which cell heterogeneity influences LNP delivery is understudied. Relating heterogeneity to LNP delivery could identify genes or cell states that promote or prevent LNP delivery or, alternatively, could allow tailoring of mRNA therapies to cell subsets that drive disease. Several lines of evidence led us to hypothesize that cells exhibit heterogeneous responses to LNPs and that these responses influence the efficiency of mRNA therapeutics. One line of evidence is that cell heterogeneity can drive metabolic[33] or immunological responses[34]. Metabolic changes can increase[27] or decrease[28] LNP delivery, and increasing the robustness of immunological responses decreases LNP delivery[29]. Another line of evidence shows that cells respond heterogeneously to hydrogels[35], which are synthetic biomaterials. One caveat is that hydrogels are chemically distinct from and much larger than nanoparticles. Finally, LNP tropism to hepatocytes, endothelial cells and Kupffer cells can be tuned[10–13,36,37] by modifying LNP chemistry without using targeting ligands such as antibodies, peptides or aptamers. These data suggest that cells can sense differences in LNP chemical composition.

An ideal way to test this hypothesis would be to measure LNP biodistribution (that is, LNPs entering cells), functional delivery (that is, delivered mRNA translated into functional protein) and the

[1]Wallace H. Coulter Department of Biomedical Engineering, Georgia Institute of Technology and Emory University School of Medicine, Atlanta, GA, USA. [2]Parker H. Petit Institute for Bioengineering and Biosciences, Georgia Institute of Technology, Atlanta, GA, USA. [3]Department of Chemical Engineering, Georgia Institute of Technology, Atlanta, GA, USA. [4]Woodruff School of Mechanical Engineering, Georgia Institute of Technology, Atlanta, GA, USA. [5]These authors contributed equally: Curtis Dobrowolski, Kalina Paunovska. ✉e-mail: james.dahlman@bme.gatech.edu

cellular response to LNPs, all in single cells. An ideal readout would also be generated in transcriptionally distinct single cells, thereby enabling analysis of on- and off-target delivery in any combination of cells, including rare cell types or cell types without validated fluorescence-activated cell sorting (FACS) markers. However, techniques to generate multiomic readouts of nanoparticle delivery in single cells are not well established. These criteria led us to design single-cell nanoparticle targeting-sequencing (SENT-seq), which quantifies the biodistribution of many chemically distinct LNPs, measured with DNA barcodes, the functional delivery of mRNA, measured as protein using DNA-encoded antibodies, and the transcriptome of transfected cells, measured with single-cell RNA sequencing (scRNA-seq).

Single-cell readouts of gene expression, mRNA delivery and DNA barcode delivery

We designed SENT-seq to work with single-cell suspensions mixed with 20 μm carboxy-coated magnetic polymer beads conjugated to DNA through an amine-reactive oligonucleotide using N-hydroxysulfosuccinimide sodium salt. We designed the beads with two orthogonal capture sequences: one bound a universal sequence in all the LNP-carried DNA barcodes, and the other, a poly-T, captured poly-A tagged cell hash oligonucleotide antibodies[38] and endogenous mRNA with poly-A tails (Fig. 1a and Supplementary Fig. 1a). We reasoned that by adding orthogonal capture sequences to the same bead in defined ratios, we could customize the proportion of sequencing reads—and therefore sensitivity—of LNP-delivered DNA barcodes relative to the mRNA and protein readouts. To evaluate whether distinct capture signals orthogonally quantified LNP barcodes and mRNA, we coated beads with the LNP barcode and poly-T capture sequences, mixed them with 10 μM of complementary fluorescent probes for 15 min (Fig. 1b), washed them and then quantified the mean fluorescence intensity (MFI) of the probes by flow cytometry. Beads that were mixed with fluorescent probes complementary to the barcode capture sequence or, separately, the poly-T capture sequence led to increased MFI in the appropriate channels, whereas beads mixed with both fluorescent probes resulted in a strong signal in both channels (Fig. 1c). As a negative control, we quantified the MFI after mixing both probes with beads without the capture sequences and found no signal (Fig. 1c). We then performed a titration experiment, decreasing the amount of barcode while increasing the amount of mRNA, or vice versa (Fig. 1d). The relationship between the barcode and mRNA concentrations and subsequent mapped reads was linear across five orders of magnitude (Fig. 1e).

We then combined this readout with an LNP DNA barcoding-based workflow (Fig. 1f). Specifically, LNP-1, with chemical structure 1, was formulated to carry mRNA encoding a glycosylphosphatidylinositol (GPI)-anchored camelid single variable domain on a heavy chain (VHH) antibody (anchored-VHH, aVHH) and DNA barcode 1 at a lipid/nucleic acid mass ratio of 10:1 using microfluidic mixing[39]. This process was repeated N times so that LNP-N, with chemical structure N, carried aVHH mRNA and DNA barcode N. By using DNA barcodes to quantify the biodistribution of many LNPs simultaneously, SENT-seq can test a large, chemically diverse LNP library without the need to sacrifice, sort and sequence single cells from hundreds of mice. The aVHH, barcode and mass ratio were rationally designed: the VHH domain was linked to a GPI anchor to induce cell-surface aVHH expression, allowing aVHH+ cells to be detected with an anti-camelid VHH antibody[40], the DNA barcode (Supplementary Fig. 1a) was sequence-optimized to reduce the genomic DNA background and chemically modified to reduce nuclease-mediated degradation[41], and the 10:1 mass ratio successfully delivered mRNA while retaining enough barcode to read[11]. After administering the barcoded LNP library to mice, we isolated the liver and digested it into a single-cell suspension, which we then mixed with the DNA-conjugated 20 μm carboxy-coated magnetic polymer beads.

We then used SENT-seq to analyse for the presence of LNP-delivered DNA barcodes, functional LNP-mediated mRNA delivery and the transcriptome using 24 chemically distinct LNPs in vivo. To create the 24 LNPs (Supplementary Fig. 2a), we varied four traits that can alter LNP activity[42]: the identity of three of the constituents (ionizable lipid, cholesterol or polyethylene glycol (PEG) lipid) and the molar ratio of all four constituents. We then characterized the hydrodynamic diameter and stability of all 24 LNPs by dynamic light scattering. LNPs with a unimodal diameter distribution and a hydrodynamic diameter between 50 and 150 nm (Supplementary Fig. 2b,c) were pooled and dialysed in 1× phosphate buffered saline (PBS). Additionally, we measured the encapsulation efficiency of all pooled LNPs individually and found that they were all over 60% (Supplementary Fig. 2d). As a control, we measured the hydrodynamic diameter of the pooled LNPs and found it to be within the range of diameters of the LNPs constituting the pool, suggesting that the LNPs did not aggregate after mixing (Supplementary Fig. 2b). Of the 24 LNPs, the 19 that met the inclusion criteria were administered as a pool to mice at a total nucleic acid dose of 1.5 mg per kg body weight (0.08 mg per kg body weight per LNP, on average). As a negative sequencing control, we added unencapsulated barcodes (also termed naked barcodes), which enter cells far less efficiently than barcodes encapsulated by LNPs[9].

Fifteen hours after administration, which is sufficient time for LNP-mediated aVHH mRNA delivery to produce aVHH protein, we isolated cells from the liver, digested them into a single-cell suspension and sorted live cells by FACS (Supplementary Fig. 3). We modified a Microwell-seq protocol[43] to read out both mRNA and barcode at the single-cell level. We then analysed the scRNA-seq data using the R package Seurat[44] and plotted the data from 12,828 distinct single cells using t-distributed stochastic neighbour embedding (t-SNE). The number of cells per condition, reads per cell, genes per cell, total reads and a breakdown of the percentage of reads mapped to cellular mRNA were consistent with previous publications[43] and are shown in Supplementary Fig. 4a. We found that hepatocytes, endothelial cells, Kupffer cells, hepatic stellate (Ito) cells and other hepatic cell types separated into transcriptionally distinct subtypes when plotted using t-SNE (Fig. 2a) and uniform manifold approximation and projection (UMAP) techniques (Supplementary Fig. 4b), based on differentially expressed genes (Supplementary Fig. 4c,d). We then quantified functional mRNA delivery (that is, the presence of aVHH protein) at the single-cell level by sequencing DNA-tagged anti-aVHH antibodies and overlaid these readouts on the t-SNE plot. As a control, we assessed the validity of our aVHH cut-off (≥4 reads per cell) by quantifying aVHH+ cells in control mice treated with 1× PBS and found that 10.9% of cells passed this threshold (PBS mean aVHH reads per cell: 0.5, PBS median aVHH reads per cell: 0; LNP pool mean aVHH reads per cell: 5.4, LNP pool median aVHH reads per cell: 5), indicating that our cut-off was stringent (Supplementary Fig. 4e). As another control, we compared the percentage of aVHH+ cells measured by the DNA-tagged anti-aVHH antibodies (Supplementary Fig. 5a–f) with the percentage of aVHH+ cells identified using traditional flow cytometry (Supplementary Fig. 5g). We found 1.4-fold more aVHH+ cells using the DNA-tagged anti-aVHH antibodies than by using flow cytometry when looking at the whole hepatic population (Supplementary Fig. 5h), suggesting that DNA-tagged antibodies may provide a more sensitive readout of functional mRNA delivery than flow cytometry.

We observed aVHH protein in all 17 cell subtypes (Fig. 2b), including subtypes that are not identifiable using established FACS markers; these data demonstrate that measuring delivery in transcriptionally defined cells may generate a more detailed picture of on- and off-target delivery than traditional techniques. Finally, we
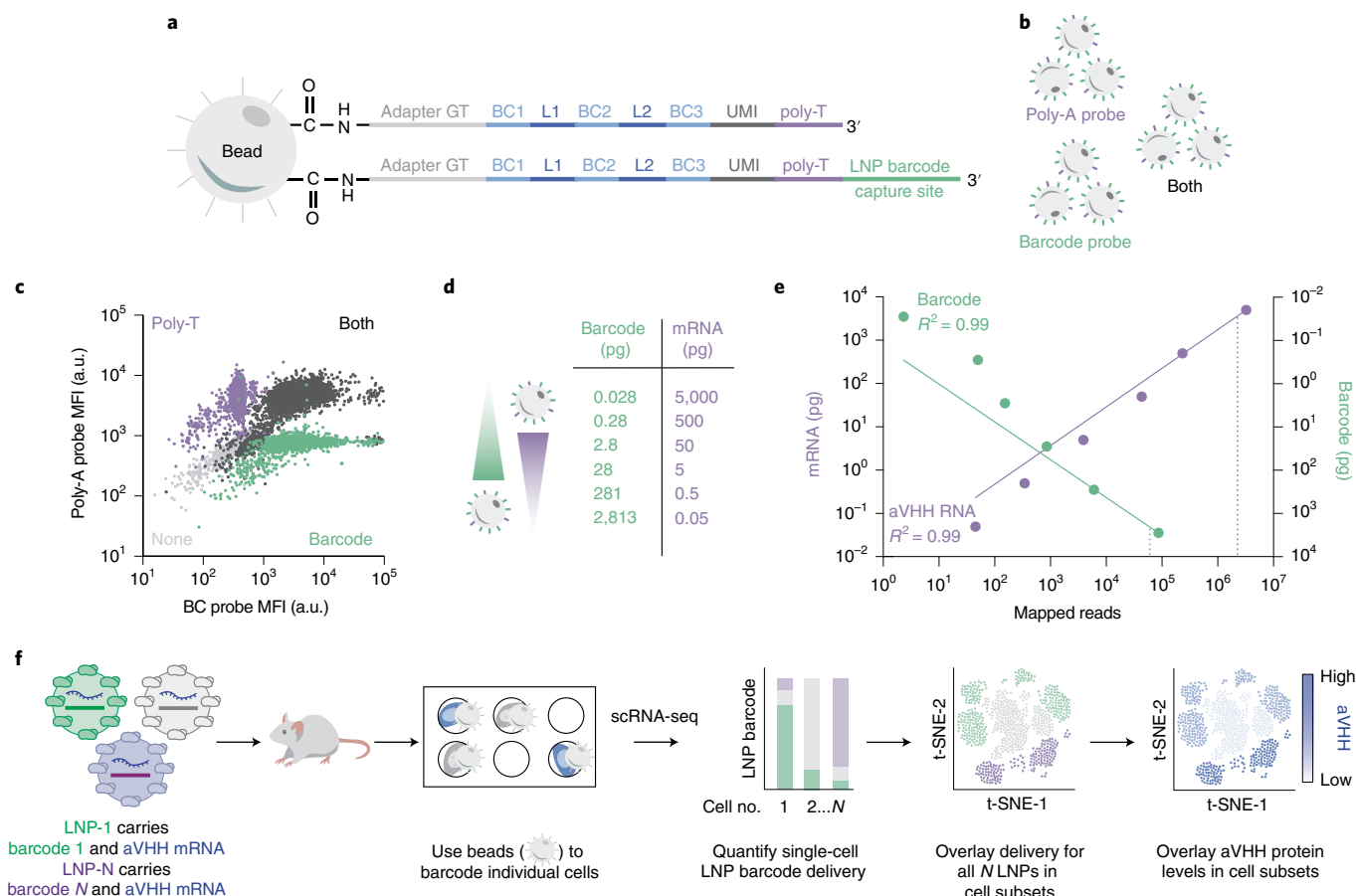
Fig. 1 | SENT-seq uses orthogonal capture sequences to generate tunable multiomic readouts. a, The sensitivity of the DNA barcode readouts relative to the biological (that is, mRNA and protein) readouts was controlled by the ratio of two orthogonal capture sequences: the barcode capture sequence and poly-T, which captured mRNA and poly-A tagged cell hash oligonucleotide antibodies. **b,c**, Beads carrying the barcode capture sequences and poly-T were mixed with the complementary fluorescent barcode probe, fluorescent poly-A probe, both or, as a negative control, none (**b**), and the MFI of each coupling was quantified (**c**). **d,e**, Beads carrying both capture sequences were mixed with varying amounts of LNP barcode or mRNA (**d**) to generate sequencing read standard curves (**e**). **f**, After formulating and injecting N chemically distinct LNPs carrying mRNA and DNA barcodes, tissues were isolated and digested into single-cell suspensions. The workflow shows delivery mediated by all N LNPs, subsequent mRNA-mediated protein production and transcriptome quantification in single cells using next-generation sequencing. BC, barcode; L, linker; UMI, unique molecular identifier.

quantified LNP barcode delivery in single cells (Fig. 2c) and over-laid the most common barcode in every cell on the t-SNE plot. As a control, we assessed the validity of our barcode cut-off (nor-malized barcode expression ≥1) and quantified the percentage of barcode-containing cells in control mice treated with 1× PBS and found that only 4.9% of cells passed this threshold (PBS mean bar-code expression: 12.2, PBS median barcode expression: 0; LNP pool mean barcode expression: 413.2, LNP pool median barcode expres-sion: 393.5). We also noted that the barcodes delivered by LNP-3, LNP-7, LNP-10 and LNP-12 were delivered in more cells than the barcodes delivered by other LNPs (Fig. 2c) and that, as expected, the negative control unencapsulated barcodes (marked by an asterisk) were delivered less efficiently than the barcodes carried by LNPs (Supplementary Fig. 6). Taking these findings together, we con-cluded that it was feasible to quantify gene expression, the presence of LNP-delivered barcodes delivered by chemically distinct LNPs and functional mRNA delivery with single-cell resolution in vivo.

Cell heterogeneity influences LNP delivery in vivo
After characterizing SENT-seq and using it to generate multiomic nanoparticle readouts, we used the data to test the hypothesis that cell heterogeneity influences LNP delivery. We first quantified LNP-mediated DNA barcode delivery by quantifying the barcode

counts in each cell, binning those counts by increments of 100 and plotting a histogram of cells with counts within each bin. Notably, different cell subtypes exhibited distinct levels of barcode reads. For example, endothelial cell subtype three (EC3) showed a sharp peak (mean: 367 counts, median: 420 counts), whereas endothelial cell subtype one (EC1) showed a broader peak (mean: 845 counts, median: 799 counts) but included cells generating as few as 100 counts and cells generating as many as 1,700 counts (Fig. 3a). To complement these DNA barcode readouts of LNP biodistribution, we analysed aVHH protein reads, which occur when LNP-delivered aVHH mRNA is translated into functional aVHH protein. We binned aVHH counts by increments of two, plotted the percentage of cells with aVHH expression values within each bin and found that the aVHH profiles for endothelial cells were similar to the endothelial cell LNP barcode delivery profiles (Fig. 3b). We noted similar qualitative trends in Kupffer cell subtype three (KC3) com-pared with Kupffer cell subtypes one (KC1) and two (KC2; Fig. 3c and Supplementary Fig. 7a), and in hepatocyte subtype two (Hep2) compared with hepatocyte subtypes one (Hep1), three (Hep3) and four (Hep4; Fig. 3d and Supplementary Fig. 7b). By contrast, Ito subtypes one (ITO1) and two (ITO2; Supplementary Figs. 7c and 8a) showed similar aVHH expression profiles but different barcode expression profiles, whereas B cell subtypes one (BC1) and two
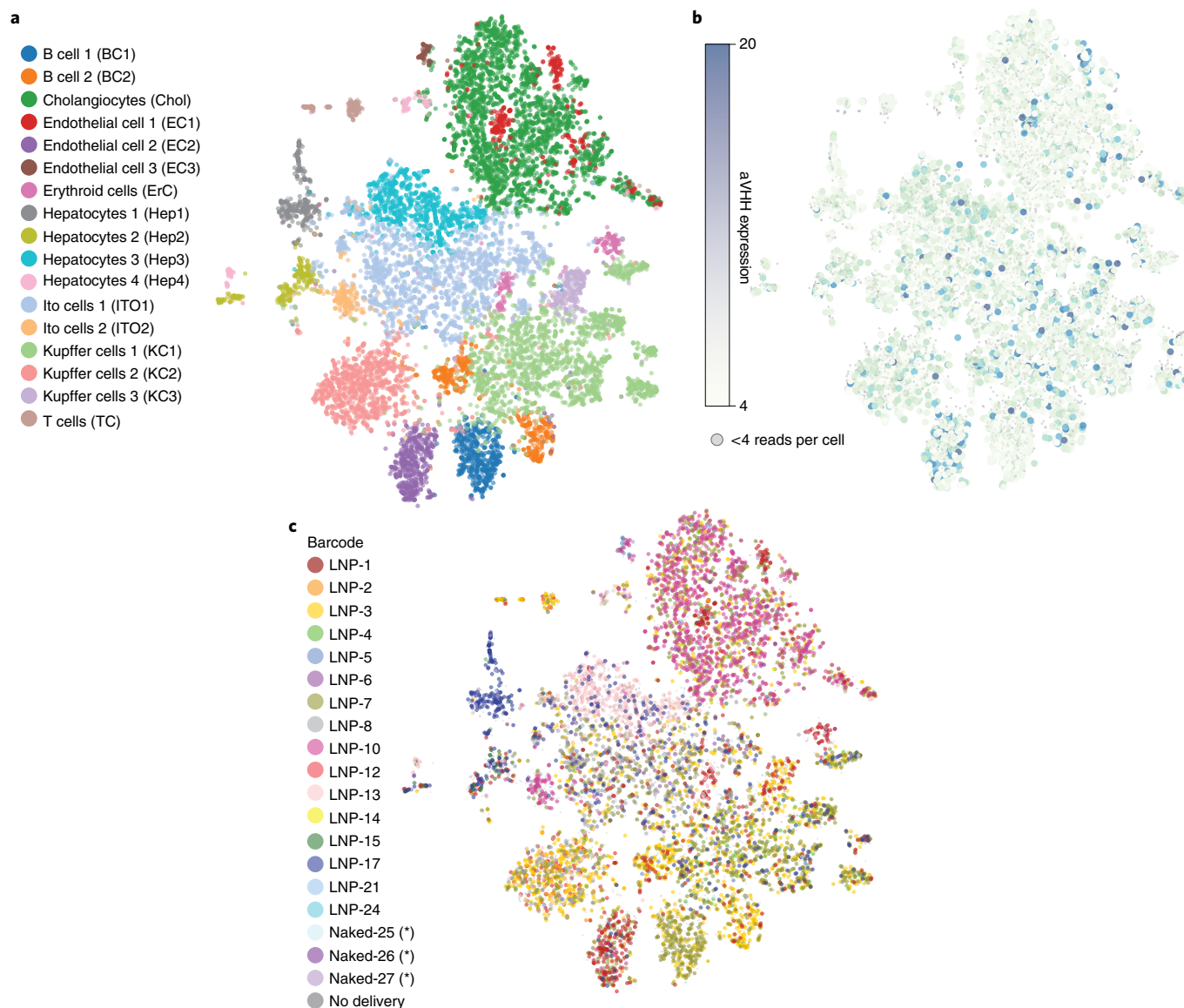
Fig. 2 | In vivo multiomic single-cell readouts of the transcriptome, functional LNP-mediated mRNA delivery and LNP-mediated DNA barcode delivery.
a, The t-SNE plot of live cells sorted from murine liver. **b**, aVHH protein expression in the same cells, overlaid on the t-SNE plot, after administration of LNPs carrying mRNA encoding aVHH. The small grey dots represent cells with less than four aVHH reads per cell. **c**, The most common barcode delivered by each of the 16, out of 24, chemically distinct LNPs, overlaid on the t-SNE plot. The 16 LNPs shown met our initial inclusion criteria and showed up in our sequenced single-cell dataset. The small dark grey dots represent cells with no barcode delivery. The asterisk represents the naked barcode.

(BC2; Supplementary Figs. 7d and 8b) showed similar aVHH and normalized barcode expression profiles.

Transcriptional analysis of cells that exhibit differential LNP delivery

These data led us to focus on endothelial cells, which showed the most distinct subtype-dependent LNP delivery and the largest statistically significant differences in the percentage of aVHH+ cells (Supplementary Fig. 5a). Notably, RNA sequencing can determine the positioning of a given endothelial cell within the vascular tree (that is, artery, capillary and vein; Fig. 4a). We therefore evaluated 20 genes previously reported to determine endothelial location in the liver vascular tree[45] and found that 16 were expressed at sufficiently high levels to analyse. Genes *Vwf* and *Thbd* were highly expressed in EC1, *Thbd* in EC2, and *Kdr*, *Vwf* and *Prss23* in EC3. These results are consistent with previous work[45] and suggest

that EC1 is present in a large artery, EC2 is part of the capillary venous system and EC3 is part of the general venous system (Fig. 4b). To better understand the global differences in the gene expression profiles, we expanded the analysis to include all genes with statistically significant differences in expression between EC1 and EC3 and, separately, between EC2 and EC3 (Fig. 4c,d). Using the DAVID database[46,47], which identifies pathways associated with a list of genes, we found that genes upregulated in EC3, relative to EC1, were either associated with transcription factor binding (P value $= 6.8 \times 10^{-3}$, GO:0008134) or with DNA binding (P value $= 4.3 \times 10^{-3}$, GO:0003677). This further suggests that the cell types were transcriptionally distinct.

Although these analyses revealed subtypes that were transcriptionally distinct, they could not identify genes that may drive differences in LNP delivery. For example, when we compared all cells in EC1 with all cells in EC3, including cells that were not targeted
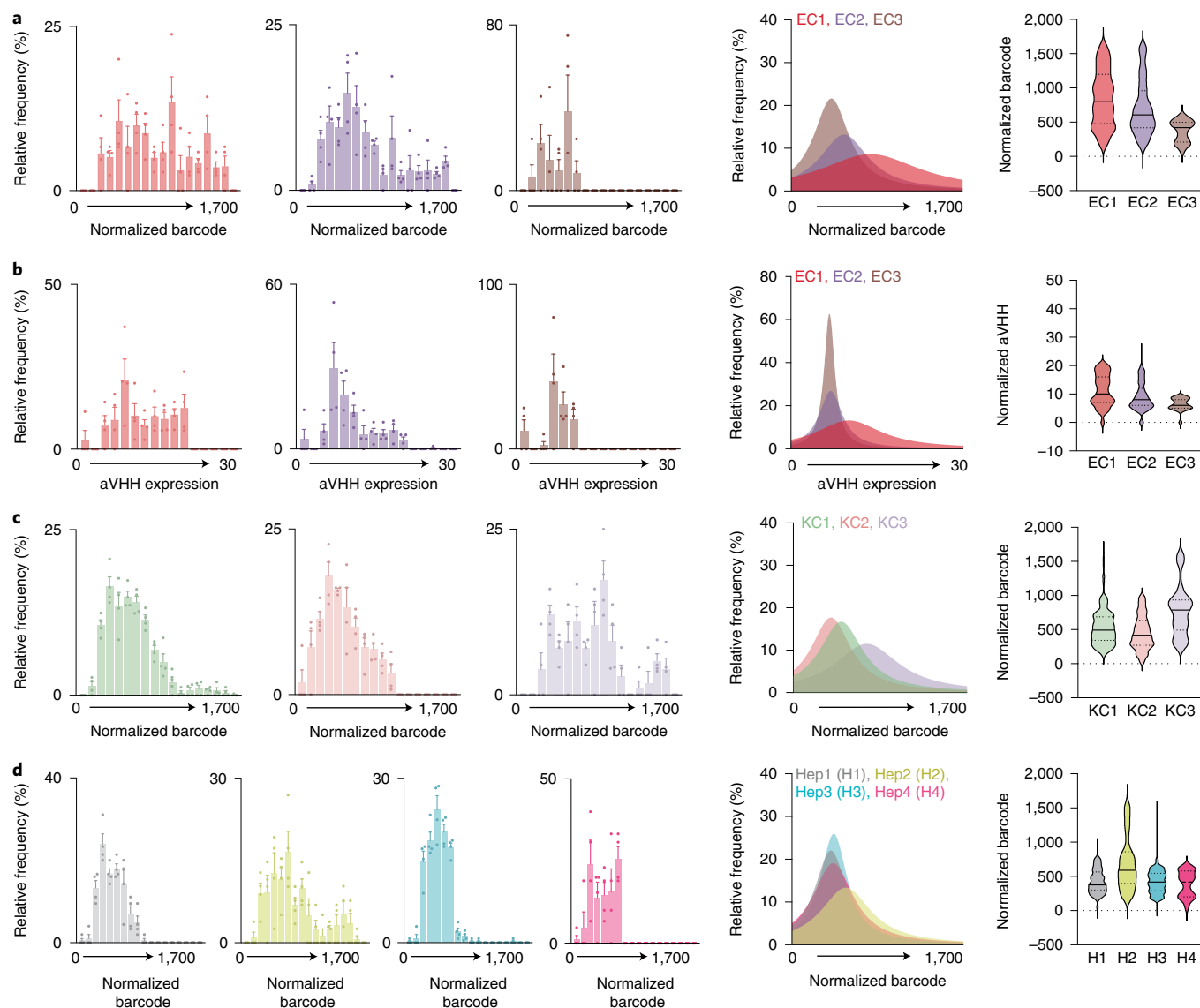
Fig. 3 | Cell subsets differentially uptake LNPs. a,b, Normalized barcode distribution (**a**) and aVHH expression (**b**) profiles for endothelial cells, along with violin plots representing the spread of the profiles. **c,d**, The normalized barcode distribution profiles and violin plots for Kupffer cells (**c**) and hepatocytes (**d**). Cell types with narrow distributions are characterized by narrow unimodal peaks of low normalized barcode delivery. Cell types with wide distributions are characterized by wide peaks or bimodal peaks of low and high normalized barcode delivery. In all cases, $n = 4$ mice per group were used; data are plotted as mean ± standard error of the mean. Histograms in **a–d** are shown with $n = 4$ dots per bar, with each dot representing a different mouse. Violin plots in **a–d** show the median (solid black line) and quartiles (dotted black lines).

by LNPs, the data included differences in basal gene expression that were unrelated to LNP delivery; this basal gene expression problem limits all RNA sequencing-based analyses of nanoparticle delivery. SENT-seq was specifically engineered to alleviate this issue by enabling us to perform three key analytical steps (Fig. 4e). First, we only compared cells in EC3 and EC1 or EC2 that had functional aVHH delivery (aVHH counts > 4, denoted as aVHH+). Second, we separately compared aVHH− (aVHH counts < 4, denoted as aVHH−) cells in EC3 with aVHH− in EC1 or EC2, thereby generating a list of genes that were differentially expressed without functional LNP delivery, that is, 'background' genes. Third, we removed the background genes from the list of differentially expressed genes in our comparisons of aVHH+ EC3 with aVHH+ EC1 or EC2. Using this approach, we identified 19 differentially expressed genes in aVHH+ EC1 and EC2, relative to EC3, that were not differentially expressed in aVHH− cells (Fig. 4f, in bold). After inputting

these 19 genes into the Search Tool for the Retrieval of Interacting Genes/Proteins (STRING)[48], we found that 11 of these genes had statistically significant interactions with each other (Fig. 4g and Supplementary Fig. 9a). Of these genes, the nodal molecules were CDK13 and CDK14, which are part of the cyclin-dependent kinase family[49]. These molecules can help to regulate cell cycle and mRNA processing[50], which may explain the increased level of functional delivery in these endothelial cell clusters. To confirm that these genes were in fact expressed differently, we also compared the overall expression levels within each cluster using a dot map. We found that the expression levels were much higher in EC1 and EC2, and much lower or even downregulated in EC3 (Fig. 4h). As noted before, EC3 also showed the lowest delivery profile, suggesting that downregulation of these genes may play a role in LNP-mediated mRNA delivery or expression. We then repeated these analyses for hepatocytes and Kupffer cells (Supplementary Fig. 9b–e) and found
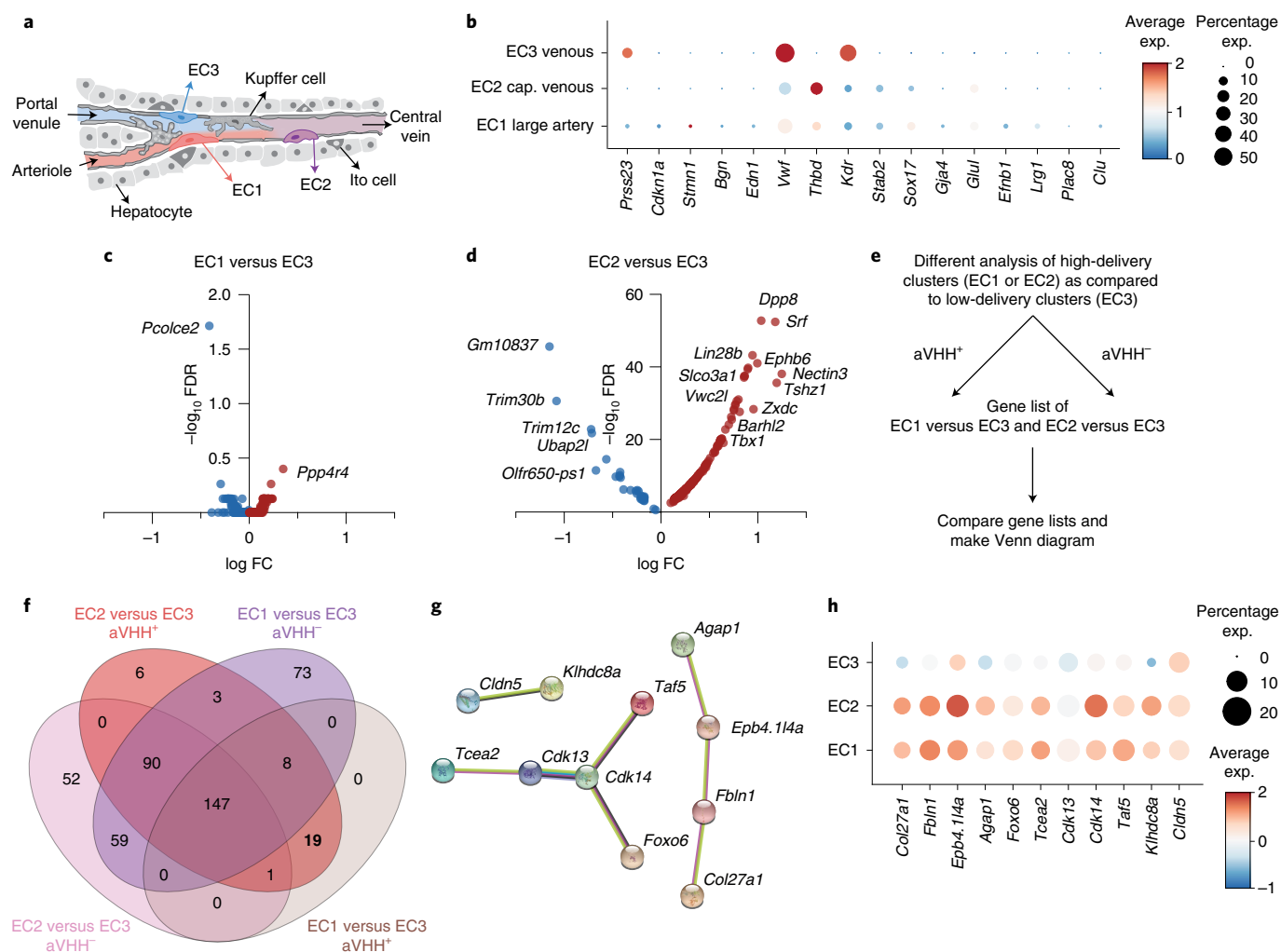
Fig. 4 | Endothelial cell subtypes show transcriptional differences that may dictate LNP-mediated mRNA delivery. a, Schematic of liver vessel morphology. **b**, Dot map showing the expression levels of 16 genes in hepatic endothelial cell differentiation. cap. venous, capillary venous; exp., expression. **c,d**, Volcano plots of differentially expressed genes in EC1 as compared with in EC3 (**c**) and in EC2 as compared with in EC3 (**d**). FC, fold change; FDR, false discovery rate. Red colour represents upregulated genes. Blue colour represents downregulated genes. **e**, Differential analysis workflow for EC clusters to identify genes. **f**, Venn diagram of differentially expressed genes found in EC1 and EC2, compared with in EC3, after separation based on aVHH expression. **g**, STRING analysis of the 19 differentially expressed genes found in aVHH^{+} cells in EC clusters 1 and 2 yielded 11 genes with statistically significant interactions. **h**, Dot map of the expression levels of differentially expressed genes in EC1, EC2 and EC3 with significant interactions.

significantly fewer genes differentially expressed in the aVHH^{+} cells that were not differentially expressed in the aVHH^{−} cells.

Quantifying LNP tropism with single-cell resolution

These results demonstrate that cell subsets differentially interact with LNPs, which led us to hypothesize that chemically distinct LNPs could exhibit different tropisms. We therefore plotted the normalized barcode counts for all 17 cell subtypes as both an average (Fig. 5a) and sum (Fig. 5b). As a control, we analysed unencapsulated barcodes and found that they were delivered less efficiently than barcodes encapsulated in LNPs. To understand the relationship between DNA barcodes and aVHH protein expression, we plotted the average normalized barcode expression against average aVHH expression for each single-cell population. We found that barcode expression increased with aVHH expression (Supplementary Fig. 10). We also generated a dot plot showing the relative (represented by the colour of the dot) and percentage (represented by the size of the dot) expression for both aVHH and normalized barcode (Supplementary Fig. 11) and noted the same trend.

Consistent with our original overlay of the most represented barcodes on the t-SNE plot (Fig. 2c), we noted that LNP-3, LNP-7, LNP-10 and LNP-12 were overrepresented, compared with other LNPs. We subsequently plotted (1) the normalized barcode counts for each individual LNP (Fig. 5c–f and Supplementary Fig. 12) and (2) the aVHH expression for each individual LNP (Fig. 5g–j and Supplementary Fig. 13) and overlaid this information on the t-SNE plot. LNP-3 was enriched in KC1 and KC2, followed by ITO1 and cholangiocytes (Fig. 5g), LNP-7 was enriched in KC1, cholangiocytes, ITO1 and BC1 (Fig. 5h), LNP-10 demonstrated strong tropism for cholangiocytes (Fig. 5i) and LNP-12 was enriched mostly in EC1 and EC2 (Fig. 5j). We reasoned that these LNPs could deliver functional mRNA with different efficiencies relative to their normalized barcode expression, or biodistribution. This rationale is supported by evidence that LNP endosomal escape is inefficient[30,31] and thus LNP biodistribution readouts can differ from functional mRNA delivery readouts. To quantify this, we plotted the ratio of aVHH protein to LNP barcode in individual cells for each LNP (Fig. 5k–n and Supplementary Fig. 14). We found that LNP-12
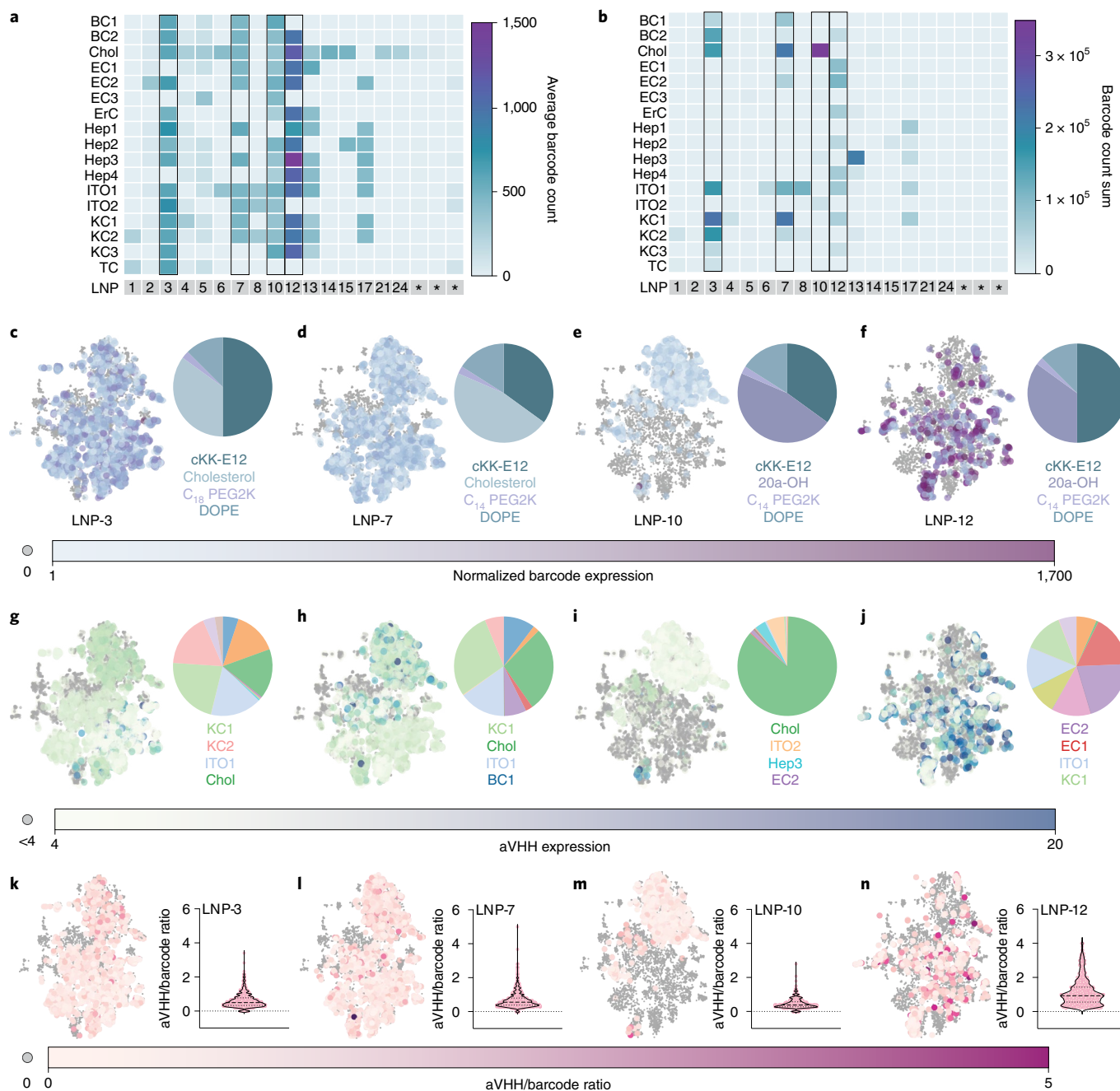
Fig. 5 | Chemically distinct LNPs exhibit different tropism within the liver microenvironment. a,b, Each LNP was formulated to contain a distinct DNA barcode, which we were able to map onto single cells. LNP barcode counts are represented in each cell cluster as either the average of barcode counts for all single cells within a cluster (**a**) or the sum of barcode counts for all single cells within a cluster (**b**). The three negative control naked barcodes are indicated by asterisks. **c–f**, The distribution and normalized barcode expression of LNP-3 (**c**), LNP-7 (**d**), LNP-10 (**e**) and LNP-12 (**f**) identified on the basis of their DNA barcode, overlaid on a t-SNE plot of 17 distinct cell subsets, shown alongside each LNPs' composition. 20a-OH, 20a-hydroxycholesterol. **g–j**, The aVHH expression profiles for LNP-3 (**g**), LNP-7 (**h**), LNP-10 (**i**) and LNP-12 (**j**), shown alongside a distribution of the cell populations that are delivered to. **k–n**, The aVHH/barcode ratio for LNP-3 (**k**), LNP-7 (**l**), LNP-10 (**m**) and LNP-12 (**n**) in all single cells where those LNPs are found.

tended to have a higher ratio of aVHH protein to barcode per cell, suggesting that the LNP, or the cell types it was transfecting, led to more functional delivery per unit of nucleic acid entering the cell.

We then identified trends in tropism and functional delivery and related them to LNP composition. We found that LNPs containing either cKK-E12, C_{14} PEG2000 (PEG2K) or 20a-hydroxycholesterol performed better than LNPs containing either cKK-E15, C_{18} PEG2K or regular cholesterol (Supplementary Fig. 15a–c). We also found

that the LNP molar ratio of 50:35:2.5:12.5 lipomer/cholesterol/PEG/phospholipid was significantly better than the other two molar ratios used in the screen (Supplementary Fig. 15d). We also observed cell-type-specific differences for LNPs containing cKK-E12 or cKK-E15 (Supplementary Fig. 16a,b), 20a-hydroxycholesterol or regular cholesterol (Supplementary Fig. 16c,d), and C_{18} PEG2K or C_{14} PEG2K (Supplementary Fig. 16e,f). Taken together, these results led us to conclude that LNPs can have differential tropism and activity within the liver microenvironment.

We then performed a series of control experiments. We compared these single-cell readouts with established bulk DNA barcoding assays[51] by measuring barcodes in aVHH+ endothelial cells (CD45−CD31+), Kupffer cells (CD45+CD68+) and hepatocytes (CD31−CD45−ASGPR+) isolated by FACS (Supplementary Fig. 3). Consistent with our single-cell readouts, LNP-3, LNP-7, LNP-10 and LNP-12 had the highest normalized barcode delivery (Supplementary Fig. 17a). We then individually injected LNP-10 and LNP-12; LNP-12 performed significantly better than LNP-10 in endothelial cells and B cells (Supplementary Fig. 17b–f), consistent with screening data (Fig. 5i–j). We evaluated the expression levels of 15 inflammation genes and found high gene expression in most single cells that received LNP-10 (Supplementary Fig. 18). We noted in our preliminary single-cell data that LNP-10 showed lower barcode (Fig. 5e,f) and aVHH expression (Fig. 5i,j) than LNP-12. These inflammation data are consistent with the hypothesis that mRNA translation may be affected by inflammation[29]. We then reasoned that cells within different metabolic zones may be differentially targeted. To test this, we focused on hepatocytes; hepatocytes closer to the portal nodes can express different markers from those closer to the central vein[52] (Supplementary Fig. 19a). We identified cells that expressed either pericentral (near the central vein, zones 1–4) or periportal (near the portal nodes, zones 5–8) metabolic zone markers to evaluate the impact of zonation on LNP delivery (Supplementary Fig. 19b–d). We found that aVHH was expressed in all zones (Supplementary Fig. 19e,f); however, within the pericentral and periportal zones, we found different distributions of the leading LNPs (Supplementary Fig. 19g–j). These results provide one early line of evidence that zonation affects LNP tropism. Finally, to control for the possibility that the differential stability of PEG lipids could lead to bias in the pooled screening system, we injected three groups of mice: (1) one group of mice received an LNP with C_{14} PEG, then later an LNP with C_{18} PEG, (2) one group received an LNP with C_{18} PEG, then later an LNP with C_{14} PEG and (3) one group was co-dosed. The evidence suggests that bias was not introduced (Supplementary Fig. 20).

Conclusions

Both FDA-approved, systemically administered siRNA therapies[3,4] that use delivery vehicles have required scientists to understand the genes that enable and enhance drug delivery. These clinical data, coupled with recent data demonstrating that LNP delivery increases[27] or decreases[28,29] depending on cell state, suggest that insights into the biology of delivery may improve clinical nanoparticles.

Here, we have reported a sequencing-based multiomic system capable of performing high-throughput in vivo nanoparticle delivery assays and analysing the cellular response to nanoparticles, all with single-cell resolution. By coupling empirical drug delivery datasets with biological readouts, SENT-seq generated several lines of evidence that cell heterogeneity influences LNP-mediated mRNA delivery. These lines of evidence were enabled by one key advantage of SENT-seq: cells are defined by their transcriptional state instead of cell surface markers. In this case, we quantified delivery to 17 cell subtypes in the liver; to our knowledge, delivery has not been previously measured in these subtypes. Furthermore, this same advantage can also serve to quantify delivery to, and therefore target, (1) rare cells, including stem cells, or (2) cells defined by a complicated transcriptional state, such as exhausted T cells[53]. Understanding LNP tropism to cell subsets could be useful as hepatocytes, immune cells, endothelial cells and other cell types continue to be subdivided into groups of cells that drive disease[45,54–56]. We are optimistic that transcriptionally defined screens will be useful now that scRNA-seq is more commonly employed to define specific transcriptional signatures in rare, disease-driving cell types. A second, related advantage is that SENT-seq may be helpful in quantifying delivery in animals that do not have

established flow antibodies for cells of interest. This is distinct from previous assays, which rely on tissue-level delivery readouts or require FACS antibody panels to isolate cells of interest, which are less common for large animals. One caveat is that these data were limited to mice, and thus SENT-seq has not yet been applied to other species. Finally, SENT-seq may be well positioned to identify LNPs that exhibit tropism changes when subtle alterations are made to their chemical composition[10–13,15], and also identify the mechanisms driving the tropism changes.

It is important to acknowledge the limitations of this work. First, the genes and pathways that promote delivery in mice may not cross over to non-human primates or humans[51]. Relatedly, the cellular responses to these LNPs may differ from the responses to polymer-, peptide- or carbohydrate-based nanoparticles as well as exosomes[57], virus-like particles[58,59] and drug delivery systems derived from protein PEG10 (ref. [60]). Thus, further work is required to understand the extent to which these genes affect delivery in other experimental models using other nanocarriers. Second, these results reveal that cell heterogeneity influences delivery to the liver and do not quantify heterogeneity in other clinically relevant organs. We anticipate that SENT-seq may help to elucidate the genes driving non-liver targeting to the lung[10,12], spleen[10,13] and bone marrow[37] using LNP-based delivery vehicles. Finally, because future nanoparticle libraries may interact with one another, it is important to include individual confirmations as well as co-dosing and sequential dosing experiments. Although additional work needs to be completed, we believe this ability to simultaneously read out high-throughput nanoparticle delivery and the cellular response to nanoparticles may lead to new datasets and insights that improve mRNA therapeutics.

Online content

Any methods, additional references, Nature Research reporting summaries, source data, extended data, supplementary information, acknowledgements, peer review information; details of author contributions and competing interests; and statements of data and code availability are available at https://doi.org/10.1038/s41565-022-01146-9.

References

1. Baden, L. R. et al. Efficacy and safety of the mRNA-1273 SARS-CoV-2 vaccine. *N. Engl. J. Med.* **384**, 403–416 (2021).
2. Polack, F. P. et al. Safety and efficacy of the BNT162b2 mRNA Covid-19 vaccine. *N. Engl. J. Med.* **383**, 2603–2615 (2020).
3. Gillmore, J. D. et al. CRISPR-Cas9 in vivo gene editing for transthyretin amyloidosis. *N. Engl. J. Med.* **385**, 493–502 (2021).
4. Adams, D. et al. Patisiran, an RNAi therapeutic, for hereditary transthyretin amyloidosis. *N. Engl. J. Med.* **379**, 11–21 (2018).
5. *Translate Bio Announces Results from Second Interim Data Analysis from Ongoing Phase 1/2 Clinical Trial of MRT5005 in Patients with Cystic Fibrosis (CF)* (Translate Bio, 2021); https://investors.translate.bio/news-releases/news-release-details/translate-bio-announces-results-second-interim-data-analysis
6. *Translate Bio Announces Pipeline Program Update* (Translate Bio, 2019); https://investors.translate.bio/news-releases/news-release-details/translate-bio-announces-pipeline-program-update
7. *Arcturus Therapeutics Announces First Quarter 2021 Company Overview and Financial Results and Provides New Clinical Data* (Arcturus Therapeutics, 2021); https://ir.arcturusrx.com/news-releases/news-release-details/arcturus-therapeutics-announces-first-quarter-2021-company
8. Altinoglu, S., Wang, M. & Xu, Q. Combinatorial library strategies for synthesis of cationic lipid-like nanoparticles and their potential medical applications. *Nanomedicine* **10**, 643–657 (2015).
9. Lokugamage, M. P., Sago, C. D. & Dahlman, J. E. Testing thousands of nanoparticles in vivo using DNA barcodes. *Curr. Opin. Biomed. Eng.* **7**, 1–8 (2018).
10. Cheng, Q. et al. Selective organ targeting (SORT) nanoparticles for tissue-specific mRNA delivery and CRISPR–Cas gene editing. *Nat. Nanotechnol.* **15**, 313–320 (2020).

11. Sago, C. D. et al. High-throughput in vivo screen of functional mRNA delivery identifies nanoparticles for endothelial cell gene editing. *Proc. Natl Acad. Sci. USA* **115**, E9944–E9952 (2018).

12. Kauffman, K. J. et al. Rapid, single-cell analysis and discovery of vectored mRNA transfection in vivo with a loxP-flanked tdTomato reporter mouse. *Mol. Ther. Nucleic Acids* **10**, 55–63 (2018).

13. Kranz, L. M. et al. Systemic RNA delivery to dendritic cells exploits antiviral defence for cancer immunotherapy. *Nature* **534**, 396–401 (2016).

14. Veiga, N. et al. Cell specific delivery of modified mRNA expressing therapeutic proteins to leukocytes. *Nat. Commun.* **9**, 4493 (2018).

15. Paunovska, K. et al. Nanoparticles containing oxidized cholesterol deliver mRNA to the liver microenvironment at clinically relevant doses. *Adv. Mater.* **31**, e1807748 (2019).

16. Lokugamage, M. P. et al. Optimization of lipid nanoparticles for the delivery of nebulized therapeutic mRNA to the lungs. *Nat. Biomed. Eng.* **5**, 1059–1068 (2021).

17. Sago, C. D. et al. Augmented lipid-nanoparticle-mediated in vivo genome editing in the lungs and spleen by disrupting Cas9 activity in the liver. *Nat. Biomed. Eng.* **6**, 157–167 (2022).

18. Akinc, A. et al. Targeted delivery of RNAi therapeutics with endogenous and exogenous ligand-based mechanisms. *Mol. Ther.* **18**, 1357–1364 (2010).

19. Akinc, A. et al. The Onpattro story and the clinical translation of nanomedicines containing nucleic acid-based drugs. *Nat. Nanotechnol.* **14**, 1084–1087 (2019).

20. Nair, J. K. et al. Multivalent *N*-acetylgalactosamine-conjugated siRNA localizes in hepatocytes and elicits robust RNAi-mediated gene silencing. *J. Am. Chem. Soc.* **136**, 16958–16961 (2014).

21. Balwani, M. et al. Phase 3 trial of RNAi therapeutic givosiran for acute intermittent porphyria. *N. Engl. J. Med.* **382**, 2289–2301 (2020).

22. Garrelfs, S. F. et al. Lumasiran, an RNAi therapeutic for primary hyperoxaluria type 1. *N. Engl. J. Med.* **384**, 1216–1226 (2021).

23. Ray, K. K. et al. Two phase 3 trials of inclisiran in patients with elevated LDL cholesterol. *N. Engl. J. Med.* **382**, 1507–1519 (2020).

24. *Alnylam Announces U.S. Food and Drug Administration Acceptance of New Drug Application for Investigational Vutrisiran for the Treatment of the Polyneuropathy of Hereditary ATTR Amyloidosis* (Alnylam, 2021); https://investors.alnylam.com/press-release?id=25811

25. Pasi, K. J. et al. Targeting of antithrombin in hemophilia A or B with RNAi therapy. *N. Engl. J. Med.* **377**, 819–828 (2017).

26. Paunovska, K., Loughrey, D. & Dahlman, J. E. Drug delivery systems for RNA therapeutics. *Nat. Rev. Genet.* **23**, 265–280 (2022).

27. Patel, S. et al. Boosting intracellular delivery of lipid nanoparticle-encapsulated mRNA. *Nano Lett.* **17**, 5711–5718 (2017).

28. Paunovska, K. et al. Increased PIP3 activity blocks nanoparticle mRNA delivery. *Sci. Adv.* **6**, eaba5672 (2020).

29. Lokugamage, M. P. et al. Mild innate immune activation overrides efficient nanoparticle-mediated RNA delivery. *Adv. Mater.* **32**, e1904905 (2019).

30. Gilleron, J. et al. Image-based analysis of lipid nanoparticle-mediated siRNA delivery, intracellular trafficking and endosomal escape. *Nat. Biotechnol.* **31**, 638–646 (2013).

31. Wittrup, A. et al. Visualizing lipid-formulated siRNA release from endosomes and target gene knockdown. *Nat. Biotechnol.* **33**, 870–876 (2015).

32. Paunovska, K. et al. A direct comparison of in vitro and in vivo nucleic acid delivery mediated by hundreds of nanoparticles reveals a weak correlation. *Nano Lett.* **18**, 2148–2157 (2018).

33. Katzenelenbogen, Y. et al. Coupled scRNA-seq and intracellular protein activity reveal an immunosuppressive role of TREM2 in cancer. *Cell* **182**, 872–885 (2020).

34. Papalexi, E. & Satija, R. Single-cell RNA sequencing to explore immune cell heterogeneity. *Nat. Rev. Immunol.* **18**, 35–45 (2018).

35. Cherry, C. et al. Computational reconstruction of the signalling networks surrounding implanted biomaterials from single-cell transcriptomics. *Nat. Biomed. Eng.* **5**, 1228–1238 (2021).

36. Paunovska, K. et al. Analyzing 2000 in vivo drug delivery data points reveals cholesterol structure impacts nanoparticle delivery. *ACS Nano* **12**, 8341–8349 (2018).

37. Sago, C. D. et al. Nanoparticles that deliver RNA to bone marrow identified by in vivo directed evolution. *J. Am. Chem. Soc.* **140**, 17095–17105 (2018).

38. Stoeckius, M. et al. Simultaneous epitope and transcriptome measurement in single cells. *Nat. Methods* **14**, 865–868 (2017).

39. Chen, D. et al. Rapid discovery of potent siRNA-containing lipid nanoparticles enabled by controlled microfluidic formulation. *J. Am. Chem. Soc.* **134**, 6948–6951 (2012).

40. Tiwari, P. M. et al. Engineered mRNA-expressed antibodies prevent respiratory syncytial virus infection. *Nat. Commun.* **9**, 3999 (2018).

41. Sago, C. D. et al. Modifying a commonly expressed endocytic receptor retargets nanoparticles in vivo. *Nano Lett.* **18**, 7590–7600 (2018).

42. Zhang, Y., Sun, C., Wang, C., Jankovic, K. E. & Dong, Y. Lipids and lipid derivatives for RNA delivery. *Chem. Rev.* **121**, 12181–12277 (2021).

43. Han, X. et al. Mapping the mouse cell atlas by Microwell-seq. *Cell* **172**, 1091–1107 (2018).

44. Hao, Y. et al. Integrated analysis of multimodal single-cell data. *Cell* **184**, 3573–3587 (2021).

45. Kalucka, J. et al. Single-cell transcriptome atlas of murine endothelial cells. *Cell* **180**, 764–779 (2020).

46. Huang, D., Sherman, B. & Lempicki, R. Systematic and integrative analysis of large gene lists using DAVID bioinformatics resources. *Nat. Protoc.* **4**, 44–57 (2009).

47. Huang, D. W., Sherman, B. T. & Lempicki, R. A. Bioinformatics enrichment tools: paths toward the comprehensive functional analysis of large gene lists. *Nucleic Acids Res.* **37**, 1–13 (2009).

48. Szklarczyk, D. et al. The STRING database in 2017: quality-controlled protein-protein association networks, made broadly accessible. *Nucleic Acids Res.* **45**, D362–D368 (2017).

49. Malumbres, M. Cyclin-dependent kinases. *Genome Biol.* **15**, 122–122 (2014).

50. Fan, Z. et al. CDK13 cooperates with CDK12 to control global RNA polymerase II processivity. *Sci. Adv.* **6**, eaaz5041 (2020).

51. Hatit, M. Z. C. et al. Species-dependent in vivo mRNA delivery and cellular responses to nanoparticles. *Nat. Nanotechnol.* **17**, 310–318 (2022).

52. Ben-Moshe, S. et al. Spatial sorting enables comprehensive characterization of liver zonation. *Nat. Metab.* **1**, 899–911 (2019).

53. Blank, C. U. et al. Defining 'T cell exhaustion'. *Nat. Rev. Immunol.* **19**, 665–674 (2019).

54. Shalek, A. K. et al. Single-cell RNA-seq reveals dynamic paracrine control of cellular variation. *Nature* **510**, 363–369 (2014).

55. Ho, D. W.-H. et al. Single-cell RNA sequencing shows the immunosuppressive landscape and tumor heterogeneity of HBV-associated hepatocellular carcinoma. *Nat. Commun.* **12**, 3684 (2021).

56. Zhang, Q. et al. Landscape and dynamics of single immune cells in hepatocellular carcinoma. *Cell* **179**, 829–845 (2019).

57. Herrmann, I. K., Wood, M. J. A. & Fuhrmann, G. Extracellular vesicles as a next-generation drug delivery platform. *Nat. Nanotechnol.* **16**, 748–759 (2021).

58. Nooraei, S. et al. Virus-like particles: preparation, immunogenicity and their roles as nanovaccines and drug nanocarriers. *J. Nanobiotechnology* **19**, 59 (2021).

59. Banskota, S. et al. Engineered virus-like particles for efficient in vivo delivery of therapeutic proteins. *Cell* **185**, 250–265 (2022).

60. Segel, M. et al. Mammalian retrovirus-like protein PEG10 packages its own mRNA and can be pseudotyped for mRNA delivery. *Science* **373**, 882–889 (2021).

61. Dahlman, J. E. et al. Barcoded nanoparticles for high throughput in vivo discovery of targeted therapeutics. *Proc. Natl Acad. Sci. USA* **114**, 2060–2065 (2017).

62. Paunovska, K. et al. Nanoparticles containing oxidized cholesterol deliver mRNA to the liver microenvironment at clinically relevant doses. *Adv. Mater.* **31**, 1807748 (2019).

63. Parekh, S., Ziegenhain, C., Vieth, B., Enard, W. & Hellmann, I. zUMIs-a fast and flexible pipeline to process RNA sequencing data with UMIs. *GigaScience* **7**, giy059 (2018).

64. Srivastava, A., Malik, L., Smith, T., Sudbery, I. & Patro, R. Alevin efficiently estimates accurate gene abundances from dscRNA-seq data. *Genome Biol.* **20**, 1–16 (2019).

65. McGinnis, C. S., Murrow, L. M. & Gartner, Z. J. DoubletFinder: doublet detection in single-cell RNA sequencing data using artificial nearest neighbors. *Cell Syst.* **8**, 329–337 (2019).

Materials and methods

Synthesis of cKK-E15. cKK-E15 was prepared as previously described[29] (Supplementary Fig. 21a–d). Briefly, 2,5-dioxopyrrolidin-1-yl N6-((benzyloxy)carbonyl)-N2-(*tert*-butoxycarbonyl)-L-lysinate (compound **1**, 20 g, 41.9 mmol) was charged in a 100 ml flask, trifluoroacetic acid (42 ml) was added slowly at 0 °C and then the mixture was stirred at room temperature for 30 min. The solvent was evaporated under reduced pressure, and then the crude product, dissolved in *N,N*-dimethylformamide (5 ml), was added dropwise to pyridine (300 ml) at 0 °C. The reaction mixture was stirred at room temperature overnight. The solvents were then evaporated under reduced pressure and the crude product washed with ethyl acetate to give pure dibenzyl (((2*S*,5*S*)-3,6-dioxopiperazine-2,5-diyl)bis(butane-4,1-diyl))dicarbamate (compound **2**, 8.4 g, 31% yield). To a solution of compound **2** in acetic acid–CH_2Cl_2 (1:1, 300 ml) was added Pd/C (10 wt.%, 3.0 g). The resulting black suspension was degassed for 5 min with hydrogen and stirred at room temperature overnight under hydrogen atmosphere. The reaction mixture was filtered through Celite and washed with MeOH. The combined filtrates were concentrated, and the crude compound was washed with ethyl acetate to yield (3*S*,6*S*)-3,6-bis(4-aminobutyl)piperazine-2,5-dione (compound **3**, 4.8 g, 98% yield; Supplementary Fig. 21a). To a solution of compound **3** (84 mg, 0.22 mmol) and tridecyloxirane (302 mg, 1.34 mmol) in EtOH (2 ml) was added triethylamine (0.12 ml, 0.88 mmol). The reaction mixture was then irradiated in a microwave reactor at 150 °C for 5 h (Supplementary Fig. 21b). Purification of the crude residue by flash column chromatography (gradient eluent: 1.0–2.0% MeOH–DCM, then 2.0–4.0% MeOH–DCM containing 0.5% NH_4OH) afforded cKK-E15 (200 mg, 78%) as a light-yellow oil. ^1H NMR (500 MHz, $CDCl_3$): $\delta = 4.02$–3.99 (m, 2H), 3.63–3.6 (m, 4H), 2.58–2.22 (m, 12H), 1.99–1.68 (m, 4H), 1.43–1.24 (m, 104H), 0.86 (t, $J = 6.9$ Hz, 12H) (Supplementary Fig. 21c). ^{13}C NMR (125 MHz, $CDCl_3$): $\delta = 169.03, 168.74, 69.98, 69.62, 67.87, 67.64, 63.35, 63.06, 61.24, 60.93, 55.82, 54.72, 35.30, 35.06, 31.94, 29.92, 29.86, 29.74, 29.71, 29.69, 29.39, 25.86, 25.84, 25.76, 25.72, 22.70, 14.13$. HRMS (ESI): *m/z* calculated for $C_{72}H_{145}N_4O_6$ 1162.1159 [M + H]$^+$, found 1162.1153 (Supplementary Fig. 21d).

aVHH mRNA synthesis. mRNA was synthesized as previously described[40]. Briefly, the GPI-anchored VHH sequence was ordered as a DNA gBlock from Integrated DNA Technologies (IDT) containing a 5′ untranslated region (UTR) with a Kozak sequence, a 3′ UTR derived from the mouse α-globin sequence and extensions to allow Gibson assembly. The sequence was human codon-optimized using the IDT website. The gBlock was then cloned into a PCR-amplified pMA7 vector through Gibson assembly using NEB Builder with 3 molar excess of insert. Gibson assembly reaction transcripts were purified on 0.8% agarose gel prior to the assembly reaction. Subsequent plasmids from each colony were Sanger-sequenced to ensure sequence identity. Plasmids were digested into a linear template using NotI-HF (New England BioLabs) overnight at 37 °C. The linearized templates were purified by ammonium acetate (Thermo Fisher Scientific) precipitation before being resuspended with nuclease-free water. In vitro transcription was performed overnight at 37 °C using a HiScribe T7 kit (NEB) following the manufacturer's instructions (full replacement of uracil with N^1-methylpseudouridine). The RNA product was treated with DNase I (Aldevron) for 30 min to remove the template and purified by lithium chloride precipitation (Thermo Fisher Scientific). The RNA transcripts were heat-denatured at 65 °C for 10 min before being capped with a cap1 structure using guanylyl transferase (Aldevron) and 2′-O-methyltransferase (Aldevron). The transcripts were then polyadenylated enzymatically (Aldevron). mRNA was then purified by lithium chloride precipitation, treated with alkaline phosphatase (NEB) and purified for a final time. Concentrations were measured using a NanoDrop spectrophotometer, and mRNA stock concentrations were between 2 and 4 mg ml^{-1}. Purified RNA products were analysed by gel electrophoresis to ensure purity. The mRNA stocks were stored at −80 °C.

Nanoparticle formulation. Nanoparticles were formulated in a microfluidic device by mixing aVHH mRNA, DNA, the ionizable lipid, PEG and cholesterol as previously described[39]. Nanoparticles were prepared with variable mole ratios of these constituents. The nucleic acid (for example, DNA barcode, mRNA) was diluted in 10 mM citrate buffer (Teknova) and loaded into a syringe (Hamilton Company). The materials making up the nanoparticles (cKK-E12, cKK-E15, cholesterol, 20a-hydroxycholesterol, C_{14} PEG2K, C_{18} PEG2K and 1,2-dioleoyl-*sn*-glycero-3-phosphoethanolamine (DOPE)) were diluted in ethanol and loaded into a second syringe. The citrate and ethanol phases were mixed in a microfluidic device using syringe pumps.

DNA barcoding. Each chemically distinct LNP was formulated to carry its own distinct DNA barcode. For example, LNP-1 carried aVHH mRNA and DNA barcode 1, whereas the chemically distinct LNP-2 carried aVHH mRNA and DNA barcode 2. The DNA barcodes were designed rationally with universal primer sites and a specific eight-nucleotide (8-nt) barcode sequence, similarly to what we previously described[61]. The DNA barcodes were single-stranded, comprised 91 nucleotides and were purchased from IDT. Briefly, the barcodes had the following characteristics and modifications: (1) the nucleotides on the 5′ and 3′ ends were modified with a phosphorothioate to reduce exonuclease degradation, (2) universal forward and reverse primer regions were included to ensure equal amplification of

each sequence, (3) seven random nucleotides were included to monitor PCR bias, (4) a droplet digital PCR (ddPCR) probe site was included for ddPCR compatibility and (5) each barcode had a unique 8-nt barcode. An 8-nt sequence can generate over 4^8 (65,536) distinct barcodes. We used only the 8-nt sequences designed to prevent sequence bleaching and reading errors on the Illumina MiniSeq sequencing machine.

Nanoparticle characterization. LNP hydrodynamic diameter and polydispersity index were measured by dynamic light scattering. The LNPs were diluted in sterile 1× PBS to a concentration of ~0.06 μg ml^{-1} and analysed. LNPs were included if they met two criteria: a diameter in the range of 20–200 nm and an autocorrelation function with only one inflection point. Particles that met these criteria were pooled and dialysed in 1× PBS (Invitrogen), and sterile-filtered through a 0.22 μm filter. The nanoparticle concentration was determined using a NanoDrop spectrophotometer (Thermo Scientific).

Encapsulation efficiency. Using two replicates for each LNP, 50 μl of a 6 ng μl^{-1} LNP-encapsulated RNA solution was added to 50 μl of a solution of 1× tris-EDTA (TE, Thermo Fisher) or a solution containing a 1:50 dilution of Triton X-100 (Sigma Aldrich). After incubating at 37 °C for 10 min, 100 μl of a solution of 1:100 RiboGreen reagent (Thermo Fisher) was added to each well. Fluorescence and absorbance were measured at an excitation wavelength of 485 nm and an emission wavelength of 528 nm using a plate reader (BioTek Synergy H4 Hybrid).

Animal experiments. All animal experiments were performed in accordance with the Georgia Institute of Technology's Institutional Animal Care and Use Committee. C57BL/6J (JAX stock number 000664) mice were purchased from the Jackson Laboratory. In all experiments, mice were aged 5–8 weeks, and $N = 4$ mice per group were injected intravenously through the lateral tail vein. The light cycle of the mouse holding room is from 07:00 to 19:00. Housing rooms are kept at ~21 °C with ~30% average humidity. The weights for all mice for all experiments are included in Supplementary Fig. 22.

Cell isolation. In all cases, mice were sacrificed 1 day after administration of the LNPs and immediately perfused with 20 ml of 1× PBS through the right atrium. The liver was isolated immediately following perfusion, minced with scissors and then placed in a digestive enzyme solution with collagenase type I (Sigma Aldrich), collagenase XI (Sigma Aldrich) and hyaluronidase (Sigma Aldrich) at 37 °C and 750 r.p.m. for 45 min. Digested tissues were passed through a 70 μm filter and red blood cells were lysed.

Cell staining. Cells were stained to identify specific cell populations and sorted using a BD FacsFusion cell sorter. The antibody clones used for staining were anti-CD31 (clone 390, BioLegend, catalogue number 102427), anti-CD45.2 (clone 104, BioLegend, cat. no. 109832), anti-CD68 (clone FA-11, Thermo Fisher, cat. no. 46-0681-82), anti-aVHH (clone 96A3F5, GenScript, cat. no. A01994), anti-ASGPR1 (clone 8D7, Santa Cruz Biosciences, cat. no. SC-52623 FITC) and live/dead cell stain kit (Thermo Fisher, cat. no. L34975). Representative gating strategies for liver cell populations are included in Supplementary Fig. 3a,b. To allow for the pooling of samples into a single device, cells were stained with a streptavidin-conjugated H-2 MHC class I antibody (clone M1/42, BioLegend, cat. no. 125502) and biotinylated cell hash oligonucleotides were added to a 0.5 μM final concentration after a single wash to remove unbound antibody. Antibodies were diluted according to the manufacturer's recommendation. All antibodies were validated for flow cytometry by the manufacturer.

PCR amplification for traditional barcoded LNP analysis. All samples were amplified and prepared for sequencing using a nested PCR protocol as previously described[62]. More specifically, 1 μl of each primer (10 μM reverse/forward) was added to 5 μl of Kapa HiFi 2× master mix, 2 μl sterile H_2O and 1 μl DNA template. The second PCR added Nextera XT chemistry, indices and i5/i7 adapter regions and used the product from the first PCR as template.

Deep sequencing. Illumina deep sequencing was performed with Illumina MiniSeq using the standard protocols suggested by Illumina. The sequencing was conducted at the Georgia Institute of Technology Molecular Evolution Core facility.

Nanoparticle data analysis and statistics. Sequencing results were processed using a custom Python-based tool to extract raw barcode counts for each tissue. These raw counts were then normalized using R script prior to further analysis. Counts for each particle were normalized to the barcoded LNP mixture injected into mice, as we previously described[9]. Data were analysed and plotted using GraphPad Prism (v 8). Flow cytometry data were analysed using FlowJo (v 10).

Data are plotted as mean ± standard error of the mean unless otherwise stated.

Synthesis of Microwell-seq barcoded beads. To generate orthogonal beads containing 10% barcode binding sequences, the following protocol was used. First, 2 ml of 50 μM amine-modified oligonucleotide was conjugated to 150 mg of 20 μm carboxy-coated magnetic beads (kbspheretech) using 200 mg

1-ethyl-3-(3-dimethylaminopropyl)carbodiimide (EDC) and N-hydroxysuccinimide (NHS) ester (Sigma Aldrich) in 6 ml of 0.1 M 2-(N-morpholino)ethanesulfonic acid (MES) overnight. The conjugated beads were then washed once in 0.1 M PBS containing 0.02% Tween-20 and then twice in TE (pH 8.0) using a magnet.

To add the three unique bead barcodes, the conjugated beads were subjected to three rounds of split-pool PCR using the cell barcode oligonucleotides according to the following protocol. The beads were washed once in double-deionized H_2O (ddH$_2$O) and resuspended in 4.5 ml of 1× Kapa HF master mix. Then, 45 μl of this suspension was aliquoted into a 96-well plate. Next, 5 μl of 50 μM of a unique cell barcode oligonucleotide, with a complementary sequence to the amine-modified oligonucleotide, was added and amplified using the following PCR program: 94 °C for 5 min, five cycles of 94 °C for 15 s, 50 °C for 4 min, 72 °C for 4 min and a final 4 °C hold. The beads were then pooled and washed twice with ddH$_2$O, and the PCR protocol was repeated twice more with the additional plates of cell barcodes. The final set of cell barcodes also contained a unique molecular identifier as well as a 15-nucleotide poly-T region for mRNA binding (Supplementary Fig. 1b). To add the LNP barcode binding site, PCR was performed following the above method; however, a mixture of poly-A and poly-A–LNP oligonucleotides at a molar ratio of 10:1 was used for priming. After the final round of PCR, the beads were pooled, washed twice in ddH$_2$O and denatured in denaturation solution composed of 150 mM sodium hydroxide solution containing 0.01% Tween 20 for 10 min at room temperature with rotation. The beads were then washed twice in denaturation solution followed by three washes with a neutralization solution containing 100 mM Tris (pH 8.0), 1 mM EDTA and 0.01% Tween 20. The final beads were stored in 1× TE containing 0.01% Tween 20 at 4 °C for up to 1 year.

Device generation and bead processing. Microwell device generation and subsequent library preparation were achieved following the protocol of Han et al. with a few modifications to accommodate cellular indexing of transcriptomes and epitopes by sequencing (CITE-seq) and the LNP barcode[43]. The microwell device was generated using a polydimethylsiloxane (PDMS) 1 million-well device (iBioChips) to create a positive imprint mould for the generation of a 5% agarose in PBS disposable device. Then, 100,000 of the isolated and pooled cells were loaded onto the agarose device and allowed to settle for 10 min until most of the cells had fallen to the bottoms of the wells. Two washes were performed with ice-cold PBS to remove any cells that did not fall into a well. The device was then placed on a strong magnet, and 1 million barcoded beads were slowly distributed over the device and allowed to incubate for 10 min so that most of the beads were immobilized in wells. Two more washes were performed to remove any unbound beads, and 1 ml cold lysis buffer (0.1 M Tris-HCl (pH 7.5), 0.5 M LiCl, 1% SDS, 10 mM EDTA and 5 mM dithiothreitol (DTT)) was added and allowed to incubate on ice for 10 min. After lysis, the device was cut out and flipped over, and the beads were removed from the wells using the magnet. The beads were pooled, washed twice with 6× SSC and given one final wash in 50 mM Tris-HCl (pH 8.0).

Library preparation. The pooled beads were then added to a reverse transcription reaction containing 200 U Moloney murine leukaemia virus reverse transcriptase (BioChain Institute), 1× reverse transcription buffer, 20 U RNAse inhibitor (NEB), 1 M betaine (Sigma), 6 mM MgCl$_2$ (Sigma), 2.5 mM DTT (Thermo Fisher), 1 mM deoxynucleotide triphosphates (NEB) and 1 μM template switch oligonucleotide primer. The beads were incubated for 90 min at 42 °C followed by a hold at 4 °C with constant shaking at 500 r.p.m. After the reverse transcriptase step, the enzyme was removed using 1× TE containing 0.5% SDS followed by washing in 1× TE containing 0.01% Tween 20 and a final wash in 100 mM Tris-HCl (pH 8.0).

Any unused single-stranded oligonucleotide was removed from the beads by treatment with 200 U exonuclease I (NEB) in 1× ExoI buffer for 60 min at 37 °C with shaking at 500 r.p.m. Following the digestion, excess ExoI was removed using the previously described TE–SDS, TE–Tween 20 and Tris-HCL (pH 8.0) washes. After the removal of ExoI, the beads were resuspended in 200 μl Platinum II Hot-Start Master Mix (Thermo Fisher) with IS-PCR, p7 Multi Barcode reverse (Rvs) and Hash p7 Rvs primers (Supplementary File 1), and the first-round PCR was performed using the following cycling conditions: 1 cycle at 94 °C for 2 min, 12 cycles of 94 °C for 15 s, 60 °C for 15 s and 68 °C for 2 min. The samples were pooled, the beads were removed and discarded, and the sample was purified using 0.6× solid-phase reversible immobilization (SPRI) beads. The long RNA fragments were collected on the SPRI beads, while the shorter barcode and hash reads remained

in the PCR supernatant; these were purified using 2.0× SPRI beads and saved for use during the final-round PCR. The RNA sample was then treated with TN5 transposase to fragment and add on sequencing handles for subsequent PCR. Both the DNA and fragmented RNA sample were then amplified by a second-round PCR with non-hot-start Q5 high-fidelity polymerase (NEB), P7 Nextera index adapters and Microwell P5 primer using the following cycling conditions: 1 cycle at 70 °C for 5 min, 12 cycles of 98 °C for 30 s, 58 °C for 30 s and 72 °C for 90 s, with a final extension at 72 °C for 2 min. The samples were then purified using 0.8× SPRI beads. Library quality control was conducted using an Agilent Bioanalyzer 2100, quantitative PCR and qubit to measure DNA prior to sequencing. Samples were then pooled at a 10:1 molar ratio of RNA to DNA, and finally sequenced on an Illumina HiSeq paired-end 150-cycle run.

Processing of single-cell data and statistics. The data were processed using zUMIs (v 2.9.7) for the RNA mapping and counting and Salmon Alevin (v 1.5.2) for the DNA barcode and cell hashes[63,64]. All samples were mapped to GRCm39, and only exonic regions were counted. All output files were loaded into Seurat (v 4.0.4), and, in summary, cells were log normalized to a scale factor of 10,000, then scaled using a linear transformation[44]. DoubletFinder (v 3) was used to identify doublets, as previously described[65]. We found 7% doublets in our data after processing with Seurat. This was followed by principal component analysis (PCA) dimensional reduction and t-SNE clustering and then the data were exported using R BioTuring Compressed Study (rBCS) for further analysis in BBrowser2 (v 2.9.23). Once in BBrowser2, the cell search tool was used to identify the cell types within each cluster, and gene expression profiles were compared within cell types of interest. Barcode counts were combined with RNA counts in Seurat and treated in a similar manner to other multimodal datasets such as CITE-seq.

Reporting summary. Further information on research design is available in the Nature Research Reporting Summary linked to this article.

Data availability
All raw sequencing data (GEO: GSE186395) are available online. All other data are provided in the main text or the Supplementary Information.

Code availability
The custom code used is available at https://github.com/Jack-Feldman/barcode_count.

Author contributions
Conceptualization: C.D., K.P. and J.E.D. Methodology: C.D., K.P. and J.E.D. Investigation: C.D., K.P., E.S.E., D.L., A.J.D.S.S., H.N., M.Z.C.H., M.P.L., Y.K., H.E.P., P.J.S. and J.E.D. Visualization: C.D., K.P. and J.E.D. Funding acquisition: J.E.D. and P.J.S. Project administration: J.E.D. Supervision: P.J.S. and J.E.D. Writing—original draft: C.D., K.P. and J.E.D. Writing—review and editing: C.D., K.P., E.S.E., D.L., A.J.D.S.S., H.N., M.Z.C.H., M.P.L., Y.K., H.E.P., P.J.S. and J.E.D.

Competing interests
C.D., K.P. and J.E.D. have filed intellectual property related to SENT-seq. J.E.D. is an advisor for GV. All other authors declare no competing interests.

Additional information
Supplementary information The online version contains supplementary material available at https://doi.org/10.1038/s41565-022-01146-9.

Correspondence and requests for materials should be addressed to James E. Dahlman.

Peer review information *Nature Nanotechnology* thanks the anonymous reviewers for their contribution to the peer review of this work.

Reprints and permissions information is available at www.nature.com/reprints.

nature portfolio

Corresponding author(s):   James Dahlman

Last updated by author(s): Oct 19, 2021

Reporting Summary

Nature Portfolio wishes to improve the reproducibility of the work that we publish. This form provides structure for consistency and transparency in reporting. For further information on Nature Portfolio policies, see our Editorial Policies and the Editorial Policy Checklist.

Statistics

For all statistical analyses, confirm that the following items are present in the figure legend, table legend, main text, or Methods section.

n/a	Confirmed	
☐	☒	The exact sample size (*n*) for each experimental group/condition, given as a discrete number and unit of measurement
☐	☒	A statement on whether measurements were taken from distinct samples or whether the same sample was measured repeatedly
☐	☒	The statistical test(s) used AND whether they are one- or two-sided *Only common tests should be described solely by name; describe more complex techniques in the Methods section.*
☒	☐	A description of all covariates tested
☐	☒	A description of any assumptions or corrections, such as tests of normality and adjustment for multiple comparisons
☐	☒	A full description of the statistical parameters including central tendency (e.g. means) or other basic estimates (e.g. regression coefficient) AND variation (e.g. standard deviation) or associated estimates of uncertainty (e.g. confidence intervals)
☐	☒	For null hypothesis testing, the test statistic (e.g. *F*, *t*, *r*) with confidence intervals, effect sizes, degrees of freedom and *P* value noted *Give P values as exact values whenever suitable.*
☒	☐	For Bayesian analysis, information on the choice of priors and Markov chain Monte Carlo settings
☒	☐	For hierarchical and complex designs, identification of the appropriate level for tests and full reporting of outcomes
☒	☐	Estimates of effect sizes (e.g. Cohen's *d*, Pearson's *r*), indicating how they were calculated

Our web collection on statistics for biologists contains articles on many of the points above.

Software and code

Policy information about availability of computer code

Data collection	In vivo cell populations were analyzed and isolated using the BD FacsFusion in the Georgia Institute of Technology Cellular Analysis Core. The samples were then processed as indicated in the text and library QC for deep sequencing was conducted using the Agilent Bioanalyzer 2100, qPCR, and qubit to measure DNA prior to sequencing. The final library was sequenced using a Illumina HiSeq paired-end 150-cycle run. The data were processed using zUMIs (v 2.9.7) for the RNA mapping and counting and Salmon Alevin (v1.5.2) for the DNA barcode and cell hashes. All output files were then loaded into Seurat (v 4.0.4) and data was further analyzed as indicated in the text. DoubletFinder (v3) was used to identify doublets. All code (https://github.com/Jack-Feldman/barcode_count)
Data analysis	Data were analyzed and plotted in GraphPad Prism 8. The specifics of the data analyses are described in the text. Flow cytometry data was analyzed using FlowJo v10. Sequencing data were analyzed using BBrowser2 (v2.9.23).

For manuscripts utilizing custom algorithms or software that are central to the research but not yet described in published literature, software must be made available to editors and reviewers. We strongly encourage code deposition in a community repository (e.g. GitHub). See the Nature Portfolio guidelines for submitting code & software for further information.

Data

Policy information about availability of data

All manuscripts must include a data availability statement. This statement should provide the following information, where applicable:
- Accession codes, unique identifiers, or web links for publicly available datasets
- A description of any restrictions on data availability
- For clinical datasets or third party data, please ensure that the statement adheres to our policy

All raw sequencing data is available online (GEO: GSE186395). All other data are in the main text or the supplementary materials.

Field-specific reporting

Please select the one below that is the best fit for your research. If you are not sure, read the appropriate sections before making your selection.

☒ Life sciences   ☐ Behavioural & social sciences   ☐ Ecological, evolutionary & environmental sciences

For a reference copy of the document with all sections, see nature.com/documents/nr-reporting-summary-flat.pdf

Life sciences study design

All studies must disclose on these points even when the disclosure is negative.

Sample size	For in vivo single cell RNA sequencing experiments: N = 4 mice / group were used for control mice (treated with PBS) and experimental mice (treated with an LNP pool). For validation in vivo experimental data shown in Supplementary Fig. 17b - f, and Supplementary Fig. 20 we used n = 2 mice / group for control mice (treated with PBS) and n = 4 mice / group for experimental mice treated with LNP pool. In this case, control mice were used for flow cytometry gating. Sample sizes were chosen to ensure accuracy of the data and to be able to obtain accurate statistics.
Data exclusions	None
Replication	Four biological replicates were used per condition for scRNA sequencing. scRNA sequencing data was validated using single LNP experiments, data for which is shown in Supplementary Fig. 17. Validation experiments showed that LNPs identified in the scRNA seq data as top performs, were able to perform well in single LNP experiments.
Randomization	When possible, mice were randomly selected and ensured to be the same age and sex.
Blinding	Some experiment participants were blinded (e.g., during mice injection and cell isolation). We did not blind the authors performing the analysis due to limited access to infrastructure.

Reporting for specific materials, systems and methods

We require information from authors about some types of materials, experimental systems and methods used in many studies. Here, indicate whether each material, system or method listed is relevant to your study. If you are not sure if a list item applies to your research, read the appropriate section before selecting a response.

Materials & experimental systems

n/a	Involved in the study
☐	☒ Antibodies
☒	☐ Eukaryotic cell lines
☒	☐ Palaeontology and archaeology
☐	☒ Animals and other organisms
☒	☐ Human research participants
☒	☐ Clinical data
☒	☐ Dual use research of concern

Methods

n/a	Involved in the study
☒	☐ ChIP-seq
☐	☒ Flow cytometry
☒	☐ MRI-based neuroimaging

Antibodies

Antibodies used	Antibody clones used for staining were anti-CD31 (390, BioLegend, cat# 102427), anti-CD45.2 (104, BioLegend, cat# 109832), anti-CD68 (FA-11, ThermoFisher, cat# 46-0681-82), anti-aVHH (96A3F5, GenScript, cat# A01994), anti-ASGPR1 (8D7, Santa Cruz Biosciences, cat# sc-52623 FITC) live/dead (Thermo Fisher, cat# L34975). To allow for pooling of samples into a single device, cells were stained with a streptavidin-conjugated H-2 MHC class I (M1/42, BioLegend, cat# 125502) antibody, and biotinylated cell hash oligos were added at 0.5 μM final concentration after a single wash to remove unbound antibody. Antibodies were diluted according to the manufacturer's recommendation.
Validation	anti-CD31 (BioLegend, 390): "Anti-mouse CD31 clones 390 and MEC13.3 bind to their respective non-overlapping epitopes in IgD2 of CD31. CD31 is a 130-140 kD glycoprotein, also known as platelet endothelial cell adhesion molecule (PECAM-1) and EndoCAM". anti-CD45.2 (BioLegend, 104): "CD45.2 is an alloantigen of CD45, expressed by Ly5.2 bearing mouse strains (e.g., A, AKR, BALB/c, CBA/Ca, CBA/J, C3H/He, C57BL, C57BR, C57L, C58, DBA/1, DBA/2, NZB, SWR, 129). CD45, a member of the protein tyrosine phosphatase (PTP) family, is a 180-240 kD glycoprotein expressed on all hematopoietic cells except mature erythrocytes and platelets." anti-CD68 (FA-11, BioLegend): "CD68 is an 85-115 kD member of the lysosomal-associated membrane protein (LAMP) family. It is expressed on tissue macrophages, Langerhans cells and at low levels on dendritic cells." Anti-Camelid VHH (96A3F5, GenScript): "A Camelid VHH Antibody (also called single-domain antibody, sdAb or Nanobody by Ablynx) is a peptide chain of about 110 amino acids long, comprising one variable domain of a heavy-chain antibody, these are called VHH fragments. It is produced from a hybridoma resulting from the fusion of partner and B-lymphocytes obtained from a rabbit immunized with llama sdAb." Anti-ASGPR1 (8D7, Santa Cruz Biosciences): "The 8D7 monoclonal antibody recognizes Asialoglycoprotein receptor 1 (ASGPR 1), also known as Hepatic lectin H1 (HL-1). ASGPR 1 is an approximately 42 kDA type II integral membrane protein that is expressed on the surface of hepatic cells." H-2 MHC class I (BioLegend, M1/42): "The M1/42 antibody reacts with the H-2 MHC class I alloantigens expressed on nucleated cells from mice of the a, b, d, j, k, s, and u haplotypes (Stallcup, KC et al, 1981). MHC class I is involved in antigen presentation to T cells expressing CD3/TCR and CD8 proteins." All antibodies were validated for flow cytometry by the manufacturer.

Animals and other organisms

Laboratory animals	BL/6 (C57Bl/6J) mice were acquired from Jackson Laboratories. All mice used were females between 5 and 8 weeks old. The light cycle of the mouse housing room is from 7 am to 7 pm. Housing rooms are kept at ~ 70 F with ~ 30% average humidity.
Wild animals	None
Field-collected samples	None
Ethics oversight	All animal experiments were performed in accordance with the Georgia Institute of Technology's Institutional Animal Care and Use Committee (IACUC) policy.

Note that full information on the approval of the study protocol must also be provided in the manuscript.

Flow Cytometry

Plots

Confirm that:

☒ The axis labels state the marker and fluorochrome used (e.g. CD4-FITC).

☒ The axis scales are clearly visible. Include numbers along axes only for bottom left plot of group (a 'group' is an analysis of identical markers).

☒ All plots are contour plots with outliers or pseudocolor plots.

☒ A numerical value for number of cells or percentage (with statistics) is provided.

Methodology

Sample preparation	In all cases, mice were sacrificed 1 day after administration of LNPs and immediately perfused with 20 mL of 1X PBS through the right atrium. The liver was isolated immediately following perfusion, minced with scissors, and then placed in a digestive enzyme solution with collagenase type I (Sigma Aldrich), collagenase XI (Sigma Aldrich), and hyaluronidase (Sigma Aldrich) at 37ºC and 750 rpm for 45 minutes. Digested tissues were passed through a 70 µm filter and red blood cells were lysed. Cells were stained to identify specific cell populations and sorted using the BD Facs Fusion cell sorter at the Georgia Institute of Technology Cellular Analysis Core.
Instrument	BD Facs Fusion cell sorter
Software	The data were analyzed using FlowJo (BD Biosciences)
Cell population abundance	Greater than 1000.
Gating strategy	Cells were gated on the live/dead marker to identify live cells followed by FSC-A / SSC-A to identify populations. Singlets were gated on FSC-A / FSC-W. Cells types were gated by plotting CD31 against CD45.2 to identify endothelial cells and immune cells. Hepatocytes were gated as CD31-CD45-ASGPR1+ and Kupffer cells were gated as CD45+CD68+. See supporting figure 3 for more information.

☒ Tick this box to confirm that a figure exemplifying the gating strategy is provided in the Supplementary Information.